TESTING THE ACCRETION FLOW WITH PLASMA WAVE HEATING MECHANISM FOR SAGITTARIUS A* BY THE 1.3MM VLBI MEASUREMENTS

Lei Huang[1,2,3], Rohta Takahashi[4], Zhi-Qiang Shen[2]

ABSTRACT

The vicinity of the supermassive black hole associated with the compact radio source Sagittarius (Sgr) A* is believed to dominate the observed emission at wavelengths near and shorter than ~ 1 millimeter. We show that a general relativistic accretion flow, heated via the plasma wave heating mechanism, is consistent with the polarization and recent mm-VLBI observations of Sgr A* for an inclination angle of $\sim 45°$, position angle of $\sim 140°$, and spin $\lesssim 0.9$. Structure in visibilities produced by the black hole shadow can potentially be observed by 1.3 mm-VLBI on the existing Hawaii-CARMA and Hawaii-SMT baselines. We also consider eight additional potential mm-VLBI stations, including sites in Chile and New Zealand, finding that with these the basic geometry of the emission region can be reliably estimated.

Subject headings: Galaxy: center — black hole physics — accretion: accretion disks — sub-millimeter — techniques: interferometric

1. Introduction

The compact radio source Sagittarius (Sgr) A*, residing at the Galactic center, is believed to be the best candidate of suppermassive black hole (Schödel et al. 2002; Ghez et al. 2005). Based on observations of the orbiting stars, the mass of its central object is measured

---

[1]Key Laboratory for Research in Galaxies and Cosmology, The University of Sciences and Technology of China, Chinese Academy of Sciences, Hefei 230026, China; mlhuang@ustc.edu.cn

[2]Key Laboratory for Research in Galaxies and Cosmology, Shanghai Astronomical Observatory, Chinese Academy of Sciences, Shanghai 200030, China

[3]Academia Sinica, Institute of Astronomy and Astrophysics, Taipei 106, Taiwan

[4]The Institute of Physical and Chemical Research, 2-1 Hirosawa, Wako, Saitama 351-0198, Japan

as over 4 million $M_\odot$ (Ghez et al. 2008; Gillessen et al. 2009). However, it remains to be conclusively proved that Sgr A* is a black hole, and the explanations of the broad-band emission are even controversial. Various morphology of the emission region, torus, jet, and their combinations, are provided by different models. The observations at millimeter or longer wavelengths cannot distinguish them due to the interstellar scattering. However, the interstellar scattering is becoming less severe as the observational wavelength decreases to millimeter band, so that the intrinsic size of Sgr A* has been measured at 7mm and 3mm (Bower et al. 2004; Shen et al. 2005). According to the extrapolated scattering size, the intrinsic structure of Sgr A* would be dominant, i.e., the sub-millimeter VLBI promises to produce unadulterated images of its intrinsic structure. However, lack of baselines results in poor uv-coverage, making the imaging impossible. Thus, theoretical modelling of Sgr A* will be critical to both planning and interpreting sub-millimeter VLBI observaions (Huang et al. 2007).

Recently, Doeleman et al. (2008) reported observations at 1.3 mm with a very-long-baseline interferometry (VLBI) array consisting of the Arizona Radio Observatory Sub-millimeter Telescope (SMT), Combined Array for Research in Millimeter-wave Astronomy (CARMA), and James Clerk Maxwell Telescope (JCMT). Robust detections are obtained on baseline CARMA-SMT at ~ 500 km and baseline JCMT-SMT at ~ 4500 km. An upper limit is yielded on baseline CARMA-JCMT at ~ 3000 km. Since these visibility measurements are too few to produce an image, a circular Gaussian modelling results in a full width at half maximum (FWHM) of $\sim 37^{+16}_{-10}\mu$as, with the scattering effects removed (Doeleman et al. 2008). However, also pointed out by them, this size is somewhat unexpected, because it is smaller than the 'black hole shadow' size of $\sim 50\mu$as regardless of the black hole spin (Falcke et al. 2000). It might be possible that the emission really comes from the inside of black hole shadow. On the other hand, a structure with a central black hole shadow itself, deviating from the Gaussian, might be implied by the visibility measurements.

In this paper, we present a general relativistic accretion flow model with plasma wave heating mechanism (Sec.2). The polarization observations can be well explained with appropriate viewing angle and other model parameters set for arbitrary black hole spin. We then tend to use eight potential stations for future 1.3mm VLBI measurements to perform visibility analysis (Sec.3). We perform a visibility analysis using eight potential stations for future 1.3 mm VLBI measurements. We test the images with recent 1.3 mm VLBI measurements and investigate the implications for the properties of the black hole and accetion flow (Sec.4). Comparisons to the earlier work and evaluations on the potential (u, v) coverage are given in the final Section.

2. General Relativistic Keplerian Accretion Flow

We follow the magneto-rotational-instability (MRI) driven accretion flow (Melia et al. 2001; Liu et al. 2007) where the primary mechanism for generation of turbulence and viscous stress in accretion flows supported by magnetohydrodynamics (MHD) simulations (Balbus & Hawley 1991, 1998). When deriving the basic equations of the general relativistic accretion flow, we use the energy momentum tensor $T^{\mu\nu}$ given as $T^{\mu\nu} = n(m_p + m_e)\eta u^\mu u^\nu + pg^{\mu\nu} + t^{\mu\nu} + q^\mu u^\nu + q^\nu u^\mu$ where n, u^μ, q^μ, $t^{\mu\nu}$, p, η, m_p and m_e are the rest number density, four-velocity, heat-flux four-vector, viscous tensor, pressure, relativistic enthalpy, the mass of the proton and the mass of the electron, respectively. The basic equations for the relativistic hydrodynamics are then derived from the baryon-mass conservation $\nabla_\mu(nu^\mu) = 0$, the energy-momentum conservation $\nabla_\nu T^{\mu\nu} = 0$ and an equation of state. Detailed derivations can be found in Takahashi (2007). In this study, the Boyer-Lindquist coordinate is used for the description of the Kerr metric.

Following Liu et al. (2007) and Huang et al. (2008), we introduce model parameters as the ratio of the total stress to the magnetic field energy density β_ν, the ratio of the magnetic field energy density to the gas pressure β_p, dimensionless constant for electron heating rate C_1, constant mass accretion rate $\dot{M}$, inclination angle i, and position angle Θ. An additional parameter of black hole spin a is also introduced. The mean black hole mass of $4.1 \times 10^6 M_\odot$, measured from the orbit of the short-period star SO-2 for the distance of 8.0 kpc (Ghez et al. 2008), is used. We adopt the simplified form for the viscous tensor component $t^r{}_\phi$ (Lasota 1994; Abramowicz et al. 1996)

$$t^r{}_\phi = -n(m_p + m_e)\nu\frac{A^{3/2}\Delta^{1/2}\gamma^3}{r^5}d\Omega/dr, \tag{1}$$

where $A = r^4 + r^2a^2 + 2Mra^2$, $\Delta = r^2 - 2Mr + a^2$, γ is the Lorentz factor, $\Omega = u^\phi/u^t = d\phi/dt$ is the angular velocity of the accretion flow, and ν is the kinematic viscosity coefficient. We then assume the α-viscosity as

$$\nu = \frac{\beta_\nu\beta_p p}{n(m_p + m_e)(-r\mathrm{d}\Omega/\mathrm{d}r)}, \tag{2}$$

where the product of β_ν and β_p represents the α coefficient.

Instead of assuming a Keplerian accretion flow co-rotating with the central black hole as was done in previous work, we include the radial momentum conservation in the equation set. I.e., at any radius, the radial velocity is solved by $\nabla_\mu T^{r\mu} = 0$. The angular velocity is a little lower than the Keplerian velocity outside about ten gravitational radii to the center. In small radii, the radial velocity increases significantly and the angular velocity becomes much lower than the Keplerian velocity. The accreted plasma passes through a sonic point

at a radius inside the innermost stable circular orbit, becomes super-sonic and finally crosses the event horizon of the black hole at a speed of light. We mention that we don't consider the causality of the accretion flow (Gammie & Popham 1998; Takahashi 2007). We also adopt the viscous tensor component derived from thin disk and the α-viscosity coefficient for simplicity. Such treatments are enough to generate rough dynamical structure for the accretion flow, which can be used for observational predictions at 1.3mm wavelength. For future observations at much shorter wavelengths and with higher resolution, causal viscosity should be calculated carefully to make more realistic images of the vicinity of the black hole.

Here, the viscous heating rate is assumed to be equal to the turbulence cascade rate, $\Gamma^+_{\rm vis} \sim c_s B^2/8\pi r H_\theta$, where B is the magnetic field amplitude determined by the gas pressure and assumed β_p, c_s is the sound speed, and H_θ is the angular half-thickness of the disk. The radiative cooling is considered for electrons only and the viscous heating rate for electrons is assumed to be different from that for protons, and the radiative cooling for electrons is much more effective. We adopt the heating mechanism by turbulent plasma wave (Blandford & Eichler 1987; Liu et al. 2006) for electrons as $\Gamma^+_{\rm acc} = \alpha_e k_B T_e \tau^{-1}_{\rm acc}$, where the timescale $\tau_{\rm acc} = 3C_1 r H_\theta \bar{v}_e/c_s^2$, $\alpha_e = x[(3K_3(x) + K_1(x))/4K_2(x) - 1]$ with $K_i(x)$ as the ith order modified Bessel function of dimensionless temperature x, and $\bar{v}_e$ is the mean electron speed. Therefore the energy equation for electrons becomes

$$nu^r \alpha_e k_B \frac{{\rm d}T_e}{{\rm d}r} = \Gamma^+_{\rm acc} + \Gamma^+_{ie} - \Lambda^-_{\rm rad}, \tag{3}$$

and the energy equation for both protons and electrons derived from local energy conservation $\nabla_\mu T^{t\mu} = 0$ is

$$nu^r \frac{d}{dr}[\eta \mathcal{E}(m_p + m_e)] = \Gamma^+_{\rm vis} - \Lambda^-_{\rm rad}, \tag{4}$$

where Γ^+_{ie} is the Coulomb energy exchange rate between electrons and protons and $\Lambda^-_{\rm rad}$ is the radiative cooling rate calculated from the sum of the energy losses due to the synchrotron radiation, the synchrotron self-Comptonization of the soft photons and the bremsstrahlung. The temperatures of protons and electrons can be solved with the Eq.4 and Eq.3 combined.

The dynamical structure of the accretion flow is determined by solving all the physical quantities on the equatorial plane and the scale height from the outermost radius of 10^4 Schwarzschild radii to the event horizon. We assume homogeneous distribution in the vertical direction at any radius and a configuration of magnetic field to be parallel to the velocity field in the upper side of the accretion flow and reversed in the lower side, which forms from the initial field lines in vertical structure and the shearing of the Keplerian accretion flow. Considering synchrotron emission of only thermal population of electrons together with self-absorption and birefringence effects, full general relativistic radiative transfer along ray

trajectories is then performed to give polarized images at any given frequency. Corresponding equations can be found in Huang et al. (2008) and Huang et al. (2009).

The model parameters are set in the following procedure. First of all, β_ν is fixed to be 0.7 when the turbulence saturates (Pessah et al. 2006). Secondly, the inclination angle i is fixed to be 45° as a typical value to reproduce high linear polarization in sub-millimeter band (Liu et al. 2007; Huang et al. 2008). The position angle Θ is chosen as 140°, which can make the accretion flow reproduce the observed position angle of electric vector (EVPA) from millimeter to near-infrared band (Bower et al. 2005; Macquart et al. 2006; Marrone et al. 2007; Meyer et al. 2007) with the mean external rotation measure of $\sim 5.6 \times 10^5 \mathrm{rad} \cdot \mathrm{m}^{-2}$ adopted (Marrone et al. 2007). Next, we arbitrarily set a value for spin a and choose an appropriate value for β_p. In practice, if a is set, β_p should be small enough to keep very low circular polarizations in the sub-millimeter band reported by Marrone et al. (2006). Finally, we adjust values for $\dot{M}$ and C_1 and calculate the synchrotron radiation of thermal electrons to reproduce the linear polarization degree of $\sim 10\%$ in sub-millimeter band (Aitken et al. 2000) and overall spectrum from centimeter to near-infrared band, fixing the flux density at 1.3 mm to 2.4 Jy. In practice, the linear polarization is most sensitive to $\dot{M}$ and the flux density is affected by the combination of $\dot{M}$, C_1, and β_p.

We adopt $i = 45°, \Theta = 140°$, which can explain the polarization observations well, as our fiducial model, then choose three sets of model parameters corresponding to three different spins. In detail, those parameters are $a = 0, \beta_p = 0.4, C_1 = 0.202, \dot{M} = 5 \times 10^{17} \mathrm{g} \cdot \mathrm{s}^{-1}$ for a non-rotating black hole, $a = 0.5, \beta_p = 0.2, C_1 = 0.357, \dot{M} = 3 \times 10^{17} \mathrm{g} \cdot \mathrm{s}^{-1}$ for a mildly-rotating black hole, and $a = 0.9, \beta_p = 0.1, C_1 = 0.765, \dot{M} = 1.2 \times 10^{17} \mathrm{g} \cdot \mathrm{s}^{-1}$ for a fast-rotating black hole. We show the global solutions of the three cases in Fig.1 and the spectra predicted by them in Fig.2. The observed emission bump and high linear polarization degree in the sub-millimeter band are predicted by the accretion flow. Another jet/outflow component (Liu et al. 2007), which is not shown in these figures, contributes to the emission and depolarization in millimeter and longer wavelengths. For the wavelength of 1.3mm we are interested in, we assume the emission is dominated by the accretion flow and the jet/outflow component may produce a weak depolarization and a certain change in its EVPA.

3. Potential (u, v) Coverage For 1.3MM VLBI

We consider the following eight potential mm-VLBI stations to simulate the 1.3mm VLBI observations in this paper: Hawaii (H), including JCMT and Submillimeter Array (SMA); SMTO (S); CARMA (C); the Large Millimeter Telescope (LMT, L) on Sierra Negra, Mexico; Chilean station (A), consisting of Atacama Submillimeter Telescope Experiment

(ASTE) and Atacama Large Millimeter Array (ALMA); the IRAM Plateau de Bure (PdBI, P), France; the IRAM Pico Veleta, Spain (PV, V); and a proposed station locating on Mount Cook in New Zealand (MT-COOK, M), one of the candidate positions for telescope establishment in the future. The (u, v) coverage from these stations is shown in the top-left panel of Fig.3. These stations offer a (u, v) coverage in almost all the direction and various baseline lengths. However, it takes about 11 hours to complete these tracks due to Earth rotation. Here we divide the total observing time into six parts, with the interval of $\sim$ 2hr. In Fig.3, they are shown in square(black), cross(blue), triangle(magenta), circle(violet), rhombus(green), and plus(red) symbols, respectively. from the beginning to the end. The (u, v) coverage in the same or neighbour symbol, is considered for a simultaneous observation.

We choose three typical sub-coverages from the total observation. *Sub-coverage i* is a sub-coverage during $\sim 16 - 20$hr (UT), produced by the Hawaii (JCMT included), SMTO, and CARMA, shown in triangle and circle in the top-right panel of Fig.3. This sub-coverage includes the coverage obtained in the observations by Doeleman et al. (2008). *Sub-coverage ii* is during $\sim 14 - 18$hr (UT) from all the stations considered, shown in cross and triangle in the bottom-left panel in Fig.3. In this sub-coverage, a wide range of baseline length of $\sim 0 - 5.5$Gλ in northwest-southeast direction is included. Especially, lengths of $\sim 3 - 5$Gλ are covered by baseline group AC/AL/AS. In almost its perpendicular direction, i.e. the northeast-southwest direction, comparable lengths are also covered by baselines CH, HS, and HL. Simultaneous detections on both perpendicular directions are very important to determine the geometry of the assumed accretion flow, as shown in Huang et al. (2007) and as follows. *Sub-coverage iii* is also from all the eight stations, but during $\sim 20 - 23$hr (UT), shown in rhombus and plus in the bottom-right panel. In this sub-coverage, a wide range of baseline length of $\sim 0 - 7$Gλ in near east-west direction is covered by baselines CS, CH, HS, HL, and AM. The baselines AL, AS, AC, AH, HM, CM, MS, and LM cover a wide range of directions apart from the east-west, but only in lengths of $\gtrsim 4$Gλ.

4. Visibility Analysis And Parameter Estimation

4.1. Black Hole Spin Estimation For the Fiducial Model

For the fiducial model described in Sec.2, with inclination angle $i = 45°$, position angle $\Theta = 140°$, but with three different black hole spins, $a = 0$, 0.5, and 0.9, we convolve the images with the scattering ellipse. We adopt mean FWHMs of the scattering screen of $1.39\lambda^2$ for the major angular size in milli-arc-second and $0.69\lambda^2$ for the minor one, and the orientation of $80°$ for the major axis, which is derived from size measurements in centimeter band (Shen et al. 2005). We then perform 2-dimensional Fourier transform with special

(u, v) coverage provided by those potential stations. With the sampling of *sub-coverage i*, the corresponding visibility profiles are shown in Fig.4. For each case, the scatter-broadened image is shown in the left. Its black hole shadow structure is shown as a white region at the center. The dark-red region beside the shadow shows the accretion flow emission boosted by Doppler effect. The predicted visibilities are shown in triangle and circle, with the (u, v) coverage in Doeleman et al. (2008) included. As mentioned in Fish et al. (2009), Sgr A* could be considered as observed in its quiescent state since it exhibited the total flux density lower than other measurements. These data can be compared with our predictions within 4 hours, although they were measured on two consecutive days. Their measurements of total flux density, correlated flux density on baseline CS, and correlated flux density on baseline HS are marked by filled circle, filled square, and filled triangles, respectively. The upper limit on baseline CH is marked by a downward arrow.

The models with $a = 0$ and $a = 0.5$ provide good explanations to the visibility measurements. Notice that the predicted visibilities in triangle at baselines CH and HS, in similar directions, cannot be fitted by a Gaussian profile. Clear structures of null point, or valley point, are predicted at $\sim 3G\lambda$, which are due to the existence of the black hole shadow (Miyoshi et al. 2007; Huang et al. 2007). We note that this structure may be absent in a lot of cases (see in the following). In our fiducial model, however, the appropriate lengths and directions make these two baselines, CH and HS, potential to detect the important structure, if better sensitivity can be achieved for CARMA.

When the black hole is assumed to be fast rotating, the predicted correlated flux densities on baselines CH and HS also increase. This is because that the emission region become more compact with large spin. When the black hole spin increases to 0.9, the predicted visibilities on baseline CH nearly exceed the observed upper limit. Furthermore, the structure of the valley point cannot be recognized. The emission region becomes so compact and totally dominated by the blue-shifted side. Therefore, for the fiducial model with $i = 45°, \Theta = 140°$, determined by polarization data, the 1.3mm visibility measurements prefer a black hole spin parameter of $a < 0.9$.

4.2. Orientation Estimation With 1.3mm VLBI

The fiducial model with a relatively mildly rotating black hole can reproduce recent 1.3mm visibility measurements. The orientation of the accretion flow is constrained by polarization observations, based on the assumption of a large-scale magnetic field in toroidal configuration. However, this specific orientation is not conclusive without direct imaging. In spite of the polarizations, the measurements on baselines CH and HS can be explained by

many appropriate combinations of a, i, and Θ, e.g., highly-inclined disk with $\Theta \sim 90° - 150°$ for relatively mild spin, or nearly face-on disk with any position angle and spin. Our favorite parameters are relatively mildly-rotating black hole, mild inclination angle, and position angle toward southeast. On the other hand, any model in opposite parameters, i.e., nearly face-on, nearly egde-on, position angle toward northeast, or extremely high spin, can be an extreme alternative to our favorite model.

We focus on the disk orientation, i.e., i and Θ, first. Choose one fiducial model with $a = 0.5, i = 45°, \Theta = 140°$, and set three alternative cases with $a = 0.5, i = 10°, \Theta = 140°$, $a = 0.5, i = 90°, \Theta = 140°$, and $a = 0.5, i = 45°, \Theta = 50°$. We sample the predicted visibilities with the *sub-coverage ii* mentioned in Sec.3, which covers comparable baseline lengths in almost perpendicular directions by baseline groups CH/HL/HS and AC/AL/AS. In particular, baseline AL can perform simultaneous observations with baseline HL at $\sim 4G\lambda$, and baselines AL and AS can perform quasi-simultaneous observations (difference within 4 hours) with baselines CH and HS at $\sim 3-3.5G\lambda$. The corresponding visibilities are predicted in Fig.5, shown in cross and triangle. It can be found that the visibilities predicted by the two baseline groups make big differences among all the possible cases. We can divide the visibility results into three groups: Group I, the predicted visibilities yielded by the two orthogonal baseline groups are comparable, e.g., the case shown in the top-right panel; Group II, the predicted visibilities yielded by AC/AL/AS are in higher correlated flux density compared to those yielded by CH/HL/HS, e.g., cases in the left two panels; Group III, opposite to Group II, e.g., the case in the bottom-right panel. These observations are capable of determining the basic geometry of the intrinsic emission region of Sgr A*. Detailed discussions are as follows.

If the results in Group I are obtained, the emission region is almost symmetrical to the east-west direction. It is probably the nearly face-on case, similar to that shown in the top-right panel of Fig.5. We show its visibilities by the total (u, v) coverage in the left panel of Fig.6. In such a case, the visibilities show a similar profile, with a clear valley along all directions. Baselines with appropriate length, $\sim 2 - 3G\lambda$ in this case, in any direction, such as CH, HS, CL, AL, have the potential to detect such structure. However, there are exceptions. Cases with higher inclination angle can be included in Group I, if the position angle is close to north or south. We show an example with $a = 0.5, i = 45°, \Theta = 165°$ in the right panel of Fig.6. In this case, the visibilities again show a similar profile along all directions, though for all the baselines we consider here the valley is missing. However, these profiles significantly deviate from Gaussian profiles.

If the results in Group II are obtained, the nearly face-on cases are excluded, and the position angle is estimated ranging from $\sim 80°$ to $\sim 150°$, or from $\sim -30°$ to $\sim -100°$.

The structure of valley point may be detected on baselines CH or HS at $\sim 2.5 - 3.5 \mathrm{G}\lambda$, except the highly-inclined cases, i.e., $i \gtrsim 60°$. In general, for a given inclination angle, the differences in correlated flux density between AC/AL/AS and CH/HL/HS are predicted to reach maxima at $\Theta \sim 120°$. For a given position angle, such differences are predicted to be larger with a higher inclination angle. VLBI observations reported in Doeleman et al. (2008) are insufficient to produce a unique estimate of the disk orientation in this case. However, Earth-aperture synthesis with additional VLBI stations may be able to do so. *Sub-coverage iii* is complementary to *sub-coverage ii* because of the different directions it covers. We sample the predicted visibilities with the new sub-coverage for the two cases in left panels of Fig.5. We then make the same sampling for these two cases by changing their position angles into $95°$. Predicted visibilities of all these four cases are shown in Fig.7.

Two baseline groups are considered, AM/CH/HL/HS which provides coverage on near east-west directions, and AC/AH/AL/AS/CL/LS which provides coverage from northeast to northwest. These two baseline groups can perform simultaneous observations with comparable baseline lengths but significantly different directions. In particular, baselines LS and CL track $\sim 45°$ from baseline CH $\sim 1.5 - 2.5 \mathrm{G}\lambda$. Baseline AL tracks nearly perpendicular to baseline HL at $\sim 4\mathrm{G}\lambda$. And AM and AS track nearly perpendicular to baseline AM at $\sim 5 - 5.5 \mathrm{G}\lambda$. With a position angle close to $\sim 150°$ (or $\sim -30°$), e.g., the two cases with $\Theta = 140°$, the visibilities yielded by the two baseline groups are predicted to be comparable at $\lesssim 5\mathrm{G}\lambda$, while in larger difference with higher inclination angle at $> 5\mathrm{G}\lambda$, i.e. between AC, AS, HM, and AM. If the position angle decreases from $\sim 150°$ to $\sim 80°$ (or from $\sim -30°$ to $\sim -100°$), e.g., the two cases with $\Theta = 95°$, the visibilities yielded by group AM/CH/HL/HS are predicted to become much lower than those yielded by group AC/AH/AL/AS/CL/LS. With higher inclination angle, these differences become larger, in particular, between AL and HL at $\lesssim 4\mathrm{G}\lambda$, and between HM (or AS) and AM at $\lesssim 5 - 5.5 \mathrm{G}\lambda$. In addition, the valley structure, or deviation from Gaussian may appear at baselines HL and HS at $\lesssim 3 - 4\mathrm{G}\lambda$.

With the two sub-coverages discussed above, we may make an estimation with an error bar as small as $\sim 20°$ of the position angle for an accretion flow of Group II. Furthermore, an edge-on case may be easily recognized by visibilities at $> 5\mathrm{G}\lambda$.

Cases in Group III are not preferred by the recent 1.3mm measurements. Those measurements have strictly constrained these cases with $a \lesssim 0.5$, $20° \lesssim i \lesssim 45°$, and $\Theta \sim 0°$, so that we won't discuss more in this paper. Of course, we can further use *sub-coverage iii* for confirmation.

4.3.   Black Hole Spin Estimation With 1.3 mm VLBI

Small values of black hole spin parameter are preferred by recent measurements. However, this is not conclusive because it is based on our fiducial model, with assumptions of specific electrons heating mechanism and magnetic field structure. In Yuan et al. (2009), we adopted the general radiatively inefficient accretion flow based on the work of Manmoto (2000) and Yuan et al. (2003), and found the recent measurements prefer extremely high values of black hole spin, in stark contrast to the result in this paper. Therefore, the spin parameter inferred from observational visibilities depends significantly upon the adopted model.

Given a specific model, the emission region becomes more compact with the increase of the black hole spin, so that the structure of the visibility valley, if present, moves towards longer baselines. What can be concluded from the visibility measurements is the basic geometry, e.g., compactness, or asymmetry, of the emission region. However, determining the black hole spin from this is generally model-dependent. We show the images and predicted visibilities of two cases for the fiducial model adopted in this paper (Model A) in the left column in Fig.8. For comparison, two cases for the model adopted in Yuan et al. (2009) (Model B) with the same parameters of spin and orientation are shown in the right column. It is found that the emission region of Model A with a non-rotating black hole is even more compact than that of Model B with a fast-rotating black hole, e.g., $a = 0.9$. Notice the predicted visibilies on baseline CH and HS, in circle and triangle at $\lesssim 3 - 3.5 \mathrm{G}\lambda$. and the data of recent measurements. Fast-rotating black hole is excluded by Model A, but preferred by Model B.

Such a difference is mainly caused by the different electron heating mechanism used. In Model A, the heating mechanism is dominated by turbulence in plasma wave. This heating mechanism is so effective that the electron temperature exceeds 10^{11}K in the innermost region. The angular velocity of the accretion flow is close to the Keplerian velocity, $\Omega \gtrsim 0.9\Omega_K^+$, outside the sonic point. The strong Doppler boosting in the blue-shifted side makes the emission region more compact. In Model B, the electrons are heated by a small fraction of the viscous heating. The electron temperature keeps lower than 10^{11}K even near to event horizon, except in cases with extremely fast-rotating black hole. Compared to Model A, it shows a flat profile in the innermost region, which extends the emission region with the same spin. Moreover, the angular velocity of the accretion flow is much lower than the Keplerian velocity, $\Omega \lesssim 0.6\Omega_K^+$. The much weaker Doppler effect makes the emission region more extended.

In order to make a good estimation of the black hole spin parameter, we should take advantage of the properties of the space-time geometry that are independent of configuration

of the emission region. For example, the shape, size of the black hole shadow, and its horizontal shift from the rotation axis of the black hole (Takahashi 2004) are the same for different models with the same spin parameter, as if the emission region is assumed to extend to the event horizon. Therefore, high-fidelity imaging via VLBI at mm/sub-mm wavelengths is critical for this. Detecting the innermost stable circular orbit of hot-spot structure, if exits, during flaring activity is another way to constrain the spin parameter directly (Broderick & Loeb 2005, 2006; Doeleman et al. 2009).

5. Discussion

We consider eight potential stations to simulate the future 1.3mm VLBI observations for Sgr A* to test the specific accretion flow model with plasma wave heating mechanism. These stations provide a highest angular resolution of $\sim 30\mu$as, which is comparable to the apparent angular size of the predicted black hole shadow structure. For our fiducial model with $i \sim 45°$ and $\Theta \sim 140°$, the recent 1.3mm VLBI measurements constrain its black hole spin parameter as $a \lesssim 0.9$. More detailed visibility analysis suggests that future VLBI observations can improve these estimates substantially.

5.1. Comparisons To Earlier Work

As mentioned in the previous section, the black hole parameter estimation is dependent on the specific model adopted to fit the observations. This is born out by other efforts to fit the 1.3mm-VLBI results.

Broderick et al. (2009) followed the general RIAF model but adopted a Keplerian velocity distribution. They preferred small values of black hole spin. This is different from the prediction of extremely large spin from our Model B, which may be caused by different treatments of velocity field and gravitational effect, i.e. Yuan et al. (2003) used Pseudo-Newtonian potential instead of Kerr metric. Interestingly, their likeliest values of black hole parameter, $a = 0, i = 40°, \Theta = -23°(157°)$, are consistent with those preferred in our Model A. The Keplerian, or near Keplerian, velocity field generically makes the emission region more compact, preferring small spin parameter.

Their most probable combination is with values $a = 0, i = 90°, \Theta = -18°(162°)$. This orientation is consistent with the preference of a high inclination angle and a small position angle for the same RIAF model, constrained by size measurements in 7mm and 3mm (Huang et al. 2007). However, our Model A with the same combination is excluded by ob-

servational data because it predicts too compact an image for the emission region. This is due to our use of the plasma wave heating mechanism.

There are other efforts of estimations on the black hole parameters, especially orientation, based on different observations and theoretical models. E.g., Markoff et al. (2007) derived a high inclination angle and a favorite value of $\sim 105°$ for position angle, by comparing the visibilities observed in 7mm and predicted by a jet-dominated model; Meyer et al. (2007) derived a high inclination angle and a range of $\sim 60° - 108°$ for position angle, by assuming that an orbiting blob contributes to near-infrared flares and a jet component contributes to mm-to-submm emission. These models describe morphologies at 1.3mm wavelength totally different from an accretion flow, which can only be distinguished by the future direct imaging.

5.2. Evaluations On The (u, v) Coverage

In order to obtain a good (u, v) coverage, we need simultanesous observation on baselines with various lengths and directions. According to theoretical predictions, baseline lengths of $\lesssim 3G\lambda$ are very important because the valley point structure of the visibility profile may be detected. Fortunately, there are five potential stations, Hawaii (including JCMT), CARMA, SMT, LMT, and the Chilean (including ALMA), can provide such suitable baseline lengths. Although the coverage is still poor, they can perform simultaneous observations at similar lengths but at almost perpendicular directions. The basic geometry of the emission region of Sgr A* may be estimated by them. Furthermore, ALMA provides excellent sensitivity on baselines as long as $\sim 7G\lambda$ (on baseline AH). It is expected to make a critical contribution to future sub-mm VLBI observations of Sgr A*.

The proposed station in New Zealand, MT-COOK, also makes great contribution. It provides long baselines at a large range of direction. With its participation, these eight stations cover almost all the directions at lengths of $\gtrsim 5G\lambda$. The longest baseline length of $\sim 8G\lambda$, which can provide the highest resolution, is also achieved by MT-COOK (on baselines CM and MS).

With the Earth's rotation, these eight stations produce sufficient (u, v) coverage to produce images of Sgr A*. However, it takes almost 11 hours to complete. In this paper, we treat observations within 2 hours as the simultaneous and those within 4 hours as the quasi-simultaneous. The estimate of the basic geometry of the emission region is made from the hypothetic observation of four hours duration, e.g., with *sub-coverage i* mentioned in Sec.3 adopted. Thus, we have to assume that Sgr A* is in its stable state during the entire

4-hour period. If we want to make more detailed estimates using coverage in a larger range of directions, we must assume that this stable state exists even longer. However, a number of flares have been observed in Sgr A* at 1.3mm, on timescales as short as 30 minutes. Therefore, reliable estimates can only be made when either Sgr A* is quiescent, the flaring region is subdominant at 1.3mm, or the observation lasts for $\lesssim 1$ hour (resulting in poorer coverage and less opportunity to detect the visibility valley associated with the black hole shadow).

There is one more short-coming in the (u, v) coverage. Region with baseline lengths of $\gtrsim 5\mathrm{G}\lambda$ is covered in almost all the directions. However, the most important region with baseline lengths of $\gtrsim 3\mathrm{G}\lambda$ is lack of coverage in northeast-southwest direction. During any simultaneous observation within 2 hours, coverage in two perpendicular directions can be obtained. However, at least one more direction between those two is necessary for a good estimation of the emission region geometry, also for a higher possibility of detection on the valley point structure. This can only be improved with an additional new station included, e.g., one in New Zealand.

REFERENCES

Abramowicz, M. A., Chen, X. -M., Granath, M., & Lasota, J. -P., 1996, ApJ, 471, 762

Aitken, D. K., et al. 2000, ApJ, 534, L173

Balbus, S. A., & Hawley, J. F., 1991, ApJ, 376, 214

Balbus, S. A., & Hawley, J. F., 1998, Rev. Mod. Phys., 70, 1

Blandford, E., & Eichler, D., 1987, Phys. Report, 154, 1

Bower, G. C., et al. 2004, Science, 304, 704

Bower, G. C., Falcke, H., Wright, M. C. H., & Backer D. C. 2005, ApJ, 618, L29

Broderick, A. E., & Loeb, A., 2005, ApJ, 363, 353

Broderick, A. E., & Loeb, A., 2006, ApJ, 367, 905

Broderick, A. E., Fish, V. L., Doeleman, S. S., & Loeb, A., 2009, ApJ, 697, 45

Doeleman, S. S., et al., 2008, Nat, 455, 78

Doeleman, S. S., Fish, V. L., Broderick, A. E., Loeb, A., & Rogers, A. E. E., 2009, ApJ, 698, 59

Falcke, H., Melia, F., Agol, E., 2000, ApJ, 528, L13

Fish, V. L., Broderick, A. E., Doeleman, S. S., & Loeb, A., 2009, ApJ, 692, L14

Gammie, C. F. & Popham, R., 1998, ApJ, 498, 313

Ghez, A. M., et al. 2005, ApJ, 620, 744

Ghez, A. M., et al. 2008, ApJ, 689, 1044

Gillessen, S., Eisenhauer, F., Trippe, S., Genzel, T., Martins, F., & Ott, T., 2009, ApJ, 692, 1075

Huang, L., Cai, M., Shen, Z. -Q., & Yuan, F., 2007, MNRAS, 379, 833

Huang, L., Liu, S., Shen, Z. -Q., Cai, M. J., Li, H., & Fryer C. L., 2008, ApJ, 676, L119

Huang, L., Liu, S., Shen, Z. -Q., Yuan, Y.-F., Cai, M. J., Li, H., & Fryer C. L., 2009, ApJ, 703, 557

Lasota, J.-P., 1994, in Theory of Accretion Disks-2, ed. W. J. Duschl, J. Frank, F. Meyer, E. Meyer-Hofmeister, & W. M. Tscharnuter (Dordrecht:Kluwer), 341

Liu, S., Petrosian, V., Melia, F., & Fryer, C. L., 2006, ApJ, 648, 1020

Liu, S., Qian, L., Wu, X.-B., Fryer, C. L., & Li, H., 2007, ApJ, 668, L127

Macquart, J. -P., Bower, G. C., Wright, M. C. H., Backer, D. C., Falcke, H., 2006, ApJ, 646, 111

Manmoto, T, 2000, ApJ, 534, 734

Markoff, S., Bower, G. C., Falcke, H., 2007, MNRAS, 379, 1519

Marrone, D. P., Moran, J. M., Zhao, J. -H., & Rao, R. 2006, ApJ, 640, 308

Marrone, D. P., Moran, J. M., Zhao, J. -H., & Rao, R. 2007, ApJ, 654, 57

Melia, F., Liu, S., & Coker, R. 2001, ApJ, 553, 146

Meyer, L., et al. 2007, A&A, 473, 707

Miyoshi, M., Kameno, S., Ishitsuka, J. K., Shen, Z.-Q., Takahashi R. & Horiuchi, S., 2007,
        Publ. Natl. Astron. Obs. Japan, 10, 15

Pessah, M. E., Chan, C. K., & Psaltis, D. 2006, Phys. Rev. Lett., 97, 221103

Schödel, R., et al. 2002, Nature, 419, 694

Shen, Z.-Q., Lo, K. Y., Liang, M.-C., Ho, P.T.P., & Zhao, J. -H. 2005, Nat, 438, 62

Takahashi, R., 2004, ApJ, 611, 996

Takahashi, R., 2007, MNRAS, 382, 567

Yuan, F., Quataert, E., & Narayan, R. 2003, ApJ, 598, 301

Yuan, Y.-F., Cao, X.-W., Huang, L., & Shen, Z.-Q., ApJ, 699, 722
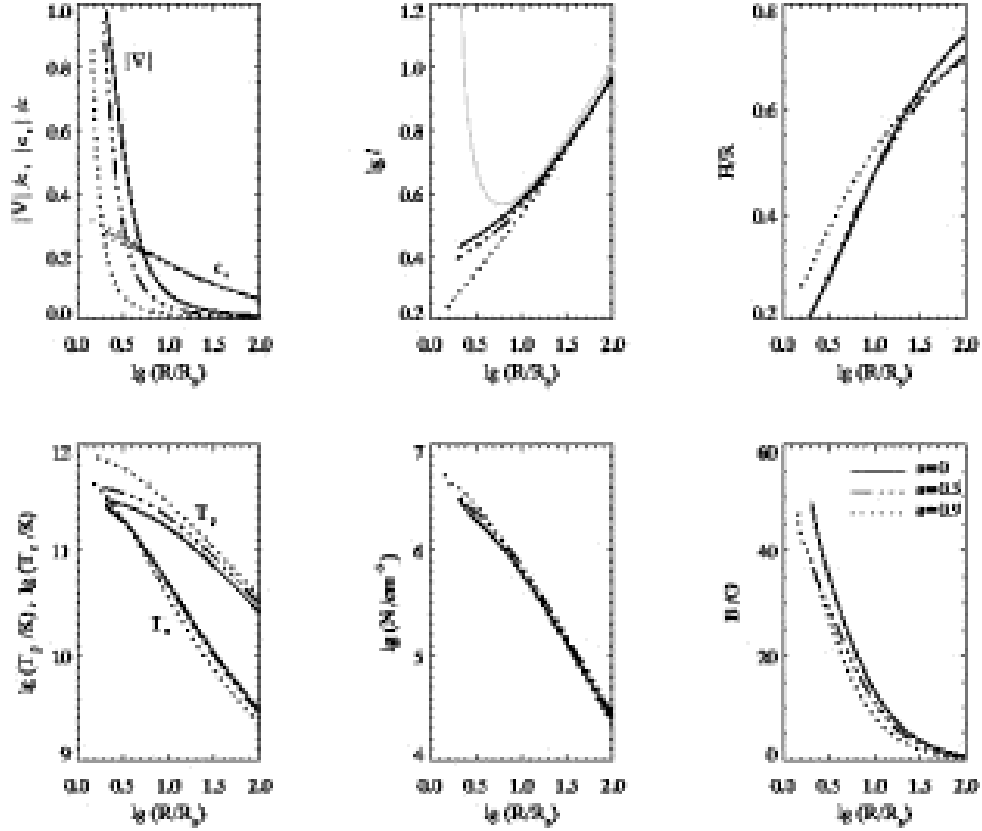
Fig. 1.— Global solutions of the accretion flow with plasma wave heating mechanism. The solid lines represent the results for $a = 0, \beta_p = 0.4, C_1 = 0.202, \dot{M} = 5 \times 10^{17} \mathrm{g} \cdot \mathrm{s}^{-1}$. The dash-three-dotted lines are for $a = 0.5, \beta_p = 0.2, C_1 = 0.357, \dot{M} = 3 \times 10^{17} \mathrm{g} \cdot \mathrm{s}^{-1}$. The dotted lines are for $a = 0.9, \beta_p = 0.1, C_1 = 0.765, \dot{M} = 1.2 \times 10^{17} \mathrm{g} \cdot \mathrm{s}^{-1}$. *Top-left*: radial velocity and sound speed; *Top-middle*: angular momentum, with the Keplerian one in solid grey line; *Top-right*: ratio of scale height to radius; *Bottom-left*: temperatures of protons and electrons; *Bottom-middle*: number density of electrons; *Bottom-right*: amplitude of magnetic field.
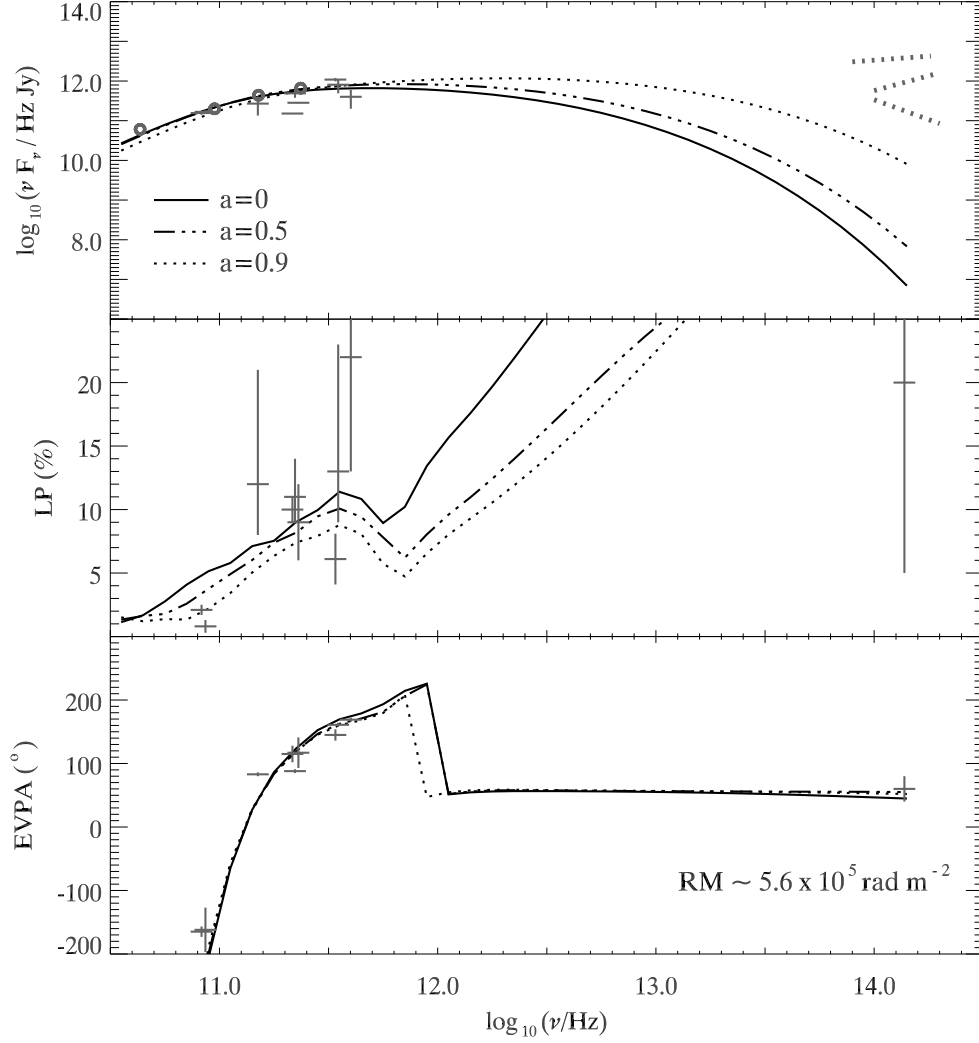
Fig. 2.— Spectrum of three accretion flow models with dynamical structures shown in Fig.1, $i = 45°$, and $\Theta = 140°$. *Top*: spectrum of total flux density of synchrotron emission; *Middle*: linear polarization degree of synchrotron emission; *Bottom*: position angle of electric vector (EVPA) with an external rotation measure of $\sim 5.6 \times 10^5 \mathrm{rad} \cdot \mathrm{m}^{-2}$ considered.
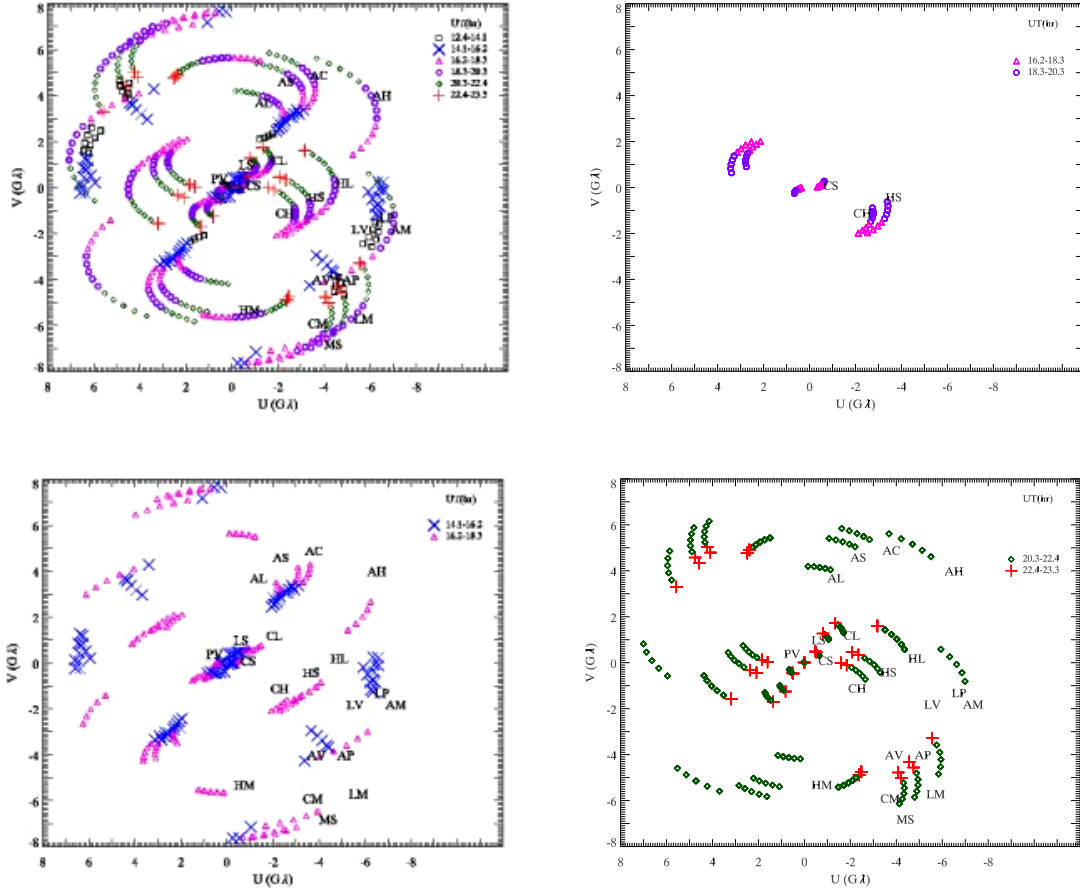
Fig. 3.— *Top-left*: (u, v) coverage produced by eight potential stations at 1.3mm wavelength. H: Hawaii, including JCMT and SMA, S: SMTO, C: CARMA, L: LMT, A: Chilean, including ASTE and ALMA, P: PdBI, V: PV, M: MT-COOK. Tracks in different parts of observational time are shown in different symbols (square, cross, triangle, circle, rhombus, and plus), with the interval of ~ 2hr. *Top-right*: *sub-coverage i* during $\sim 16 - 20$hr (UT), produced by H, S, and C. *Bottom-left*: *sub-coverage ii* during $\sim 14 - 18$hr (UT), produced by all the eight stations. *Bottom-right*: *sub-coverage iii* during $\sim 20 - 23$hr (UT), produced by all the eight stations.
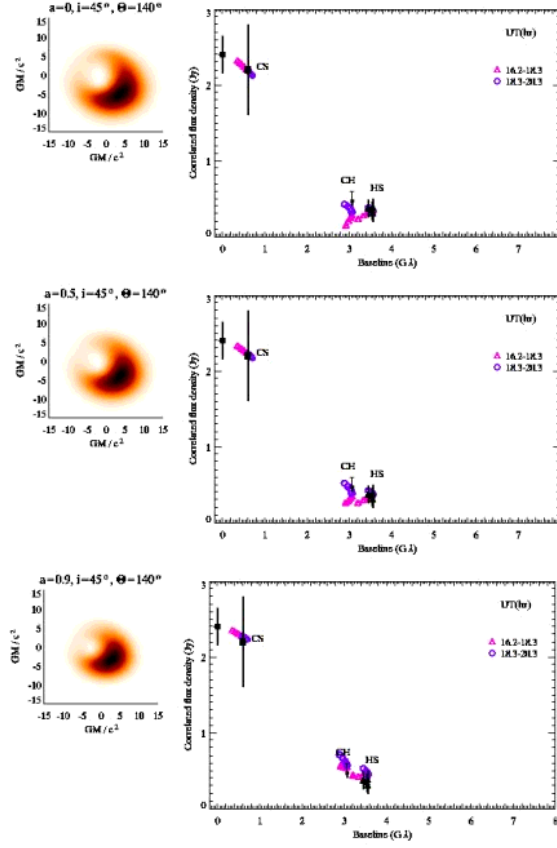
Fig. 4.— Images and visibilities predicted by the fiducial model with $a = 0$, 0.5, and 0.9, with the sampling of *sub-coverage i*. The observational data are from Doeleman et al. (2008).
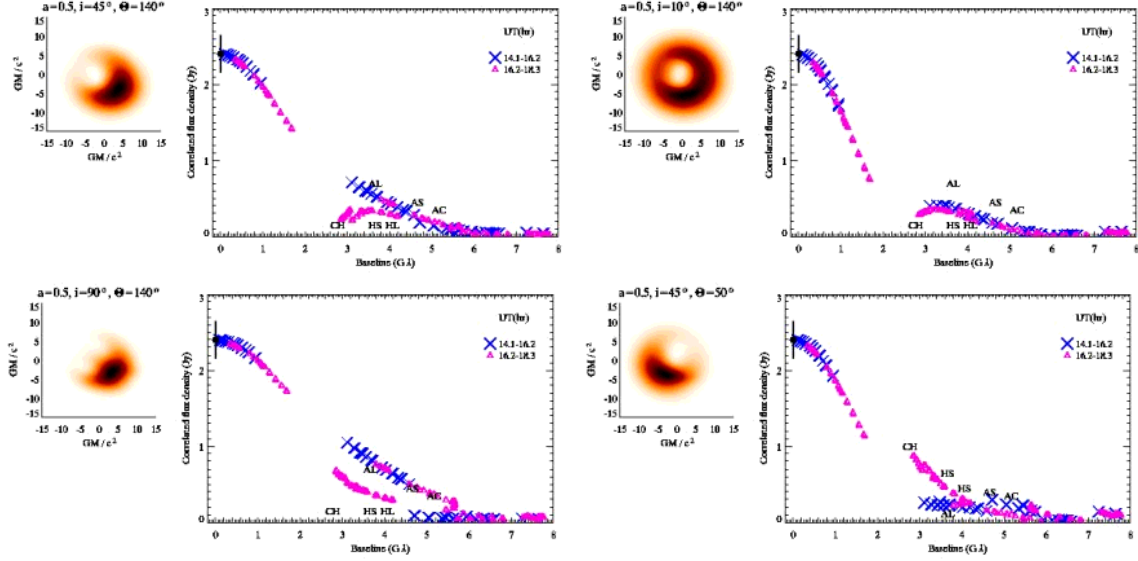
Fig. 5.— Images and visibilities predicted by four cases with $a = 0.5$ but different orientation, with the sampling of *sub-coverage ii*. In these four cases, the visibilities yielded by baseline group AC/AL/AS can be higher than, lower than, or comparable to the visibilities yielded by baseline group CH/HL/HS, see in context for details.
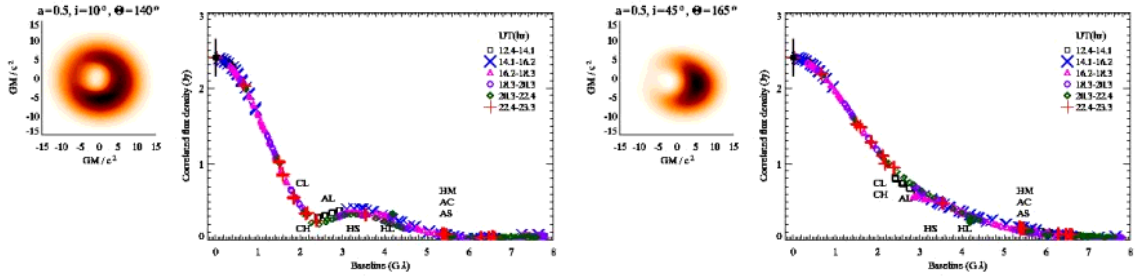

Fig. 6.— Images and visibilities predicted by two cases with $a = 0.5$ but different orientation combinations, with the sampling of the total (u, v) coverage. In both the cases, the visibilities yielded by baseline group AC/AL/AS are comparable to the visibilities yielded by baseline group CH/HL/HS.
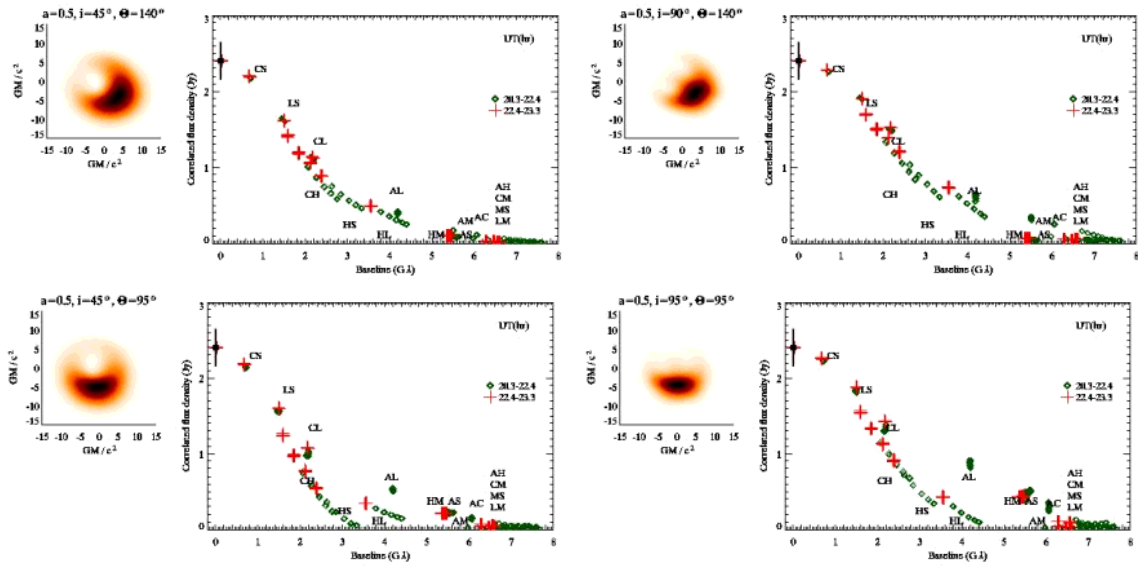
Fig. 7.— Images and visibilities predicted by four cases with $a = 0.5$ but different orientation combinations, with the sampling of *sub-coverage iii*. In these four cases, the visibilities yielded by baseline group AM/CH/HL/HS can be higher than, lower than, or comparable to the visibilities yielded by baseline group AC/AH/AL/AS/CL/LS, see in context for details.
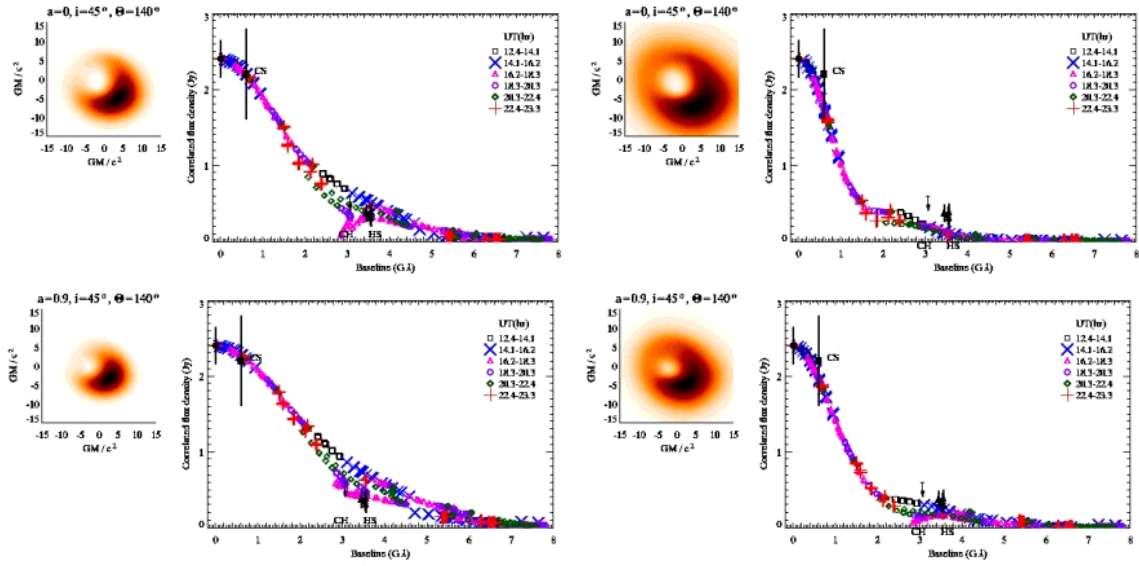
Fig. 8.— *Left*: Images and visibilities predicted by the fiducial model adopted in this paper (Model A) with $a = 0$ and 0.9, with the sampling of the total (u, v) coverage. *Right*: Images and visibilities predicted by radiatively inefficient accretion flow model adopted in Yuan et al. (2009) (Model B), with the same spin, orientation, and (u, v) sampling as the left ones.